RESEARCH ARTICLE

Error Budget of the MEthane Remote LIdar missioN and Its Impact on the Uncertainties of the Global Methane Budget

Philippe Bousquet[1] (iD), Clémence Pierangelo[2], Cédric Bacour[3], Julia Marshall[4] (iD), Philippe Peylin[1], Pradeebane Vaittinada Ayar[1], Gerhard Ehret[5], François-Marie Bréon[1], Frédéric Chevallier[1] (iD), Cyril Crevoisier[6], Fabien Gibert[6], Patrick Rairoux[7], Christoph Kiemle[5], Raymond Armante[6], Caroline Bès[2], Vincent Cassé[6] (iD), Jordi Chinaud[2], Olivier Chomette[6], Thibault Delahaye[6], Dimitri Edouart[6], Frédéric Estève[2], Andreas Fix[4] (iD), Achim Friker[8], Andrzej Klonecki[3], Martin Wirth[4], Mathias Alpers[8], and Bruno Millet[2]

[1]Laboratoire des Sciences du Climat et de l'Environnement, CEA-CNRS-UVSQ, Université Paris Saclay, Gif sur Yvette, France, [2]Centre National D'Etudes Spatiales, Toulouse, France, [3]Novoltis, Labège, France, [4]Max-Planck-Institut für Biogeochemie, Jena, Germany, [5]Deutsches Zentrum für Luft- und Raumfahrt (DLR) Oberpfaffenhofen, Institut für Physik der Atmosphäre, Weßling, Germany, [6]Laboratoire de Météorologie Dynamique, Ecole Polytechnique, Palaiseau, France, [7]Institut Lumière Matière, UMR5306 Université Lyon 1-CNRS, Université de Lyon, Villeurbanne, France, [8]Deutsches Zentrum für Luft-und Raumfahrt, Raumfahrtmanagement (DLR), Bonn, Germany

Abstract MEthane Remote LIdar missioN (MERLIN) is a German-French space mission, scheduled for launch in 2024 and built around an innovative light detecting and ranging instrument that will retrieve methane atmospheric weighted columns. MERLIN products will be assimilated into chemistry transport models to infer methane emissions and sinks. Here the expected performance of MERLIN to reduce uncertainties on methane emissions is estimated. A first complete error budget of the mission is proposed based on an analysis of the plausible causes of random and systematic errors. Systematic errors are spatially and temporally distributed on geophysical variables and then aggregated into an ensemble of 32 scenarios. Observing System Simulation Experiments are conducted, originally carrying both random and systematic errors. Although relatively small (±2.9 ppb), systematic errors are found to have a larger influence on MERLIN performances than random errors. The expected global mean uncertainty reduction on methane emissions compared to the prior knowledge is found to be 32%, limited by the impact of systematic errors. The uncertainty reduction over land reaches 60% when the largest desert regions are removed. At the latitudinal scale, the largest uncertainty reductions are achieved for temperate regions (84%) and then tropics (56%) and high latitudes (53%). Similar Observing System Simulation Experiments based on error scenarios for Greenhouse Gases Observing SATellite reveal that MERLIN should perform better than Greenhouse Gases Observing SATellite for most continental regions. The integration of error scenarios for MERLIN in another inversion system suggests similar results, albeit more optimistic in terms of uncertainty reduction.

Plain Language Summary Atmospheric methane is the second most important anthropogenic greenhouse gas. Its evolution in the atmosphere reflects the balance between its emissions and its sinks, both being still very uncertain. Observations and models are necessary to improve this situation and reduce the uncertainties associated to the global methane cycle, which is critical considering climate change. In this context, the MEthane Remote LIdar missioN (MERLIN) German-French space satellite mission, scheduled for launch in 2023, will retrieve methane atmospheric columns. MERLIN products will be integrated into atmospheric models to improve estimates of methane emissions and sinks. In this paper, we establish the first complete error budget of the future MERLIN instrument and use it to estimate the reduction of uncertainties on methane emissions that can be expected once the satellite is launched. The two main findings are that the uncertainties should be reduced on average by 60% over land, where most methane emissions are located, and that MERLIN should perform better than the main methane sounder currently on orbit for most continental regions.

1. Introduction

Atmospheric methane is a potent greenhouse gas (GHG), responsible for about 20% of the additional radiative forcing due to human activities since the industrial revolution (Ciais et al., 2013). It received increasing

Crevoisier, Fabien Gibert, Patrick Rairoux, Christoph Kiemle, Raymond Armante, Caroline Bès, Vincent Cassé, Jordi Chinaud, Olivier Chomette, Thibault Delahaye, Dimitri Edouart, Frédéric Estève, Andreas Fix, Achim Friker, Andrzej Klonecki, Martin Wirth, Mathias Alpers, Bruno Millet

Supervision: Philippe Bousquet
Visualization: Philippe Bousquet, Clémence Pierangelo, Cédric Bacour, Jordi Chinaud, Thibault Delahaye
Writing - original draft: Philippe Bousquet, Clémence Pierangelo, Cédric Bacour, Julia Marshall, Gerhard Ehret, Cyril Crevoisier, Fabien Gibert, Patrick Rairoux, Jordi Chinaud, Thibault Delahaye, Dimitri Edouart, Achim Friker, Martin Wirth, Mathias Alpers, Bruno Millet
Writing – review & editing: Philippe Bousquet

attention in the past years because of the still much debated atmospheric concentration variations, which reflect the evolving balance between surface emissions on one side and the atmospheric and surface sinks on the other side (Kirschke et al., 2013; Nisbet et al., 2014, 2016; Saunois et al., 2017; Schaefer et al., 2016). As compared to the longer lifetime of other major GHGs such as carbon dioxide and nitrous oxide, methane, with a shorter lifetime of about 9 years (Prather et al., 2012), is a particularly appropriate target for climate change mitigation policies.

Methane emissions have various sources, mostly anthropogenic (~60%), which can be related to three processes (Saunois et al., 2016): the biogenic anaerobic degradation of organic matter by Archaea (natural wetlands and inland waters, termites, enteric fermentation and manure, rice cultivation, and waste management), thermogenic formation in the Earth crust at high temperature and pressure (natural degassing of the Earth's crust and exploitation of fossil fuels), and the pyrogenic combustion of biomass under low-O_2 conditions (biomass and biofuel burning). Total emissions are estimated at 558 Tg CH_4/year (range [554–568]) for the decade 2003–2012. Methane sinks are mainly due to oxidation by OH radicals in the troposphere (~90%) but also occur in the stratosphere (reactions with $O^{(1D)}$, OH, and Cl radicals), in the marine boundary layer (reaction with Cl radicals), and in dry soils (methanotrophy).

The estimation of methane sources and sinks can be done using approaches that can be categorized as either bottom-up (process-based model, data-driven extrapolations, and emission inventories) or top-down (atmospheric inversions; Kirschke et al., 2013). With the objective to estimate sources and sinks together with their residual uncertainties after observation assimilation, atmospheric inversions optimally combine methane atmospheric observations; some prior knowledge of emissions and sinks are generally provided by bottom-up approaches and a model of chemistry-transport linking emissions and sinks to atmospheric mole fractions, in a Bayesian way (Rodgers, 2000).

Up to the mid-2000s, atmospheric inversions relied exclusively on methane observations provided by surface networks to constrain regional to global methane emissions (Bergamaschi et al., 2005; Bousquet et al., 2006; Houweling et al., 1999). Surface networks have the advantage of delivering very precise and accurate methane observations (<0.1% errors), but they remain sparse and unevenly distributed in space and time (Dlugokencky et al., 2011). The introduction of satellite data into the field of GHG science offers a revolutionary vision of the global atmospheric distribution of these gases and has a large potential to improve our knowledge about their sources and sinks. Past and present missions using shortwave infrared include the Scanning Imaging Absorption spectrometer for Atmospheric CHartographY (SCIAMACHY on board European Space Agency's [ESA's] ENVISAT, 2002–2012; Buchwitz et al., 2006; Burrows et al., 1995; Dils et al., 2006; Frankenberg et al., 2006), Japan Aerospace Exploration Agency's satellite Greenhouse Gases Observing SATellite (GOSAT, 2009–; Butz et al., 2011; Morino et al., 2011), and, more recently, TROPOspheric Monitoring Instrument (TROPOMI) on ESA's Sentinel 5 Precursor (2017–; Hu et al., 2016). Global and regional inverse modeling of methane fluxes made use of SCIAMACHY (Bergamaschi et al., 2007, 2013; Houweling et al., 2014; Meirink et al., 2008) and GOSAT (Cressot et al., 2014; Locatelli et al., 2015; Monteil et al., 2013) satellite retrievals to infer methane emissions. The Infrared Atmospheric Sounding Interferometer (2006–), developed by the French space agency (Centre national d'études spatiales [CNES]) in collaboration with Eumetsat, and operating in the thermal infrared (Crevoisier et al., 2009), can also provide consistent surface emissions with the other data sets (Cressot et al., 2014), although with very low sensitivity to the boundary layer. More detail on past, current, and planned methane space mission can be found in (Jacob et al., 2016) and (Gerhard Ehret et al., 2017).

To date, satellite data still need improvements in precision and accuracy to become a robust actor for sources and sinks estimation in the context of climate change mitigation. For instance, the use of SCIAMACHY necessitates significant bias correction, especially after 2005 due to sensor degradation. These bias corrections vary with latitude by up to ~40 ppb and are possibly linked to clouds and aerosols (Alexe et al., 2015; Bergamaschi et al., 2009; Houweling et al., 2014). Although GOSAT retrievals still present significant unexplained biases of 4–6 ppb (Buchwitz et al., 2016) and limited sampling in cloud-covered regions and in the high-latitude winter, these measurements represent an important improvement compared to SCIAMACHY for both random and systematic errors (see Table S2 of Buchwitz et al., 2016).

In this context, the MEthane LIdar missioN (MERLIN), a joint French (CNES) and German (Deutsches Zentrum für Luft- und Raumfahrt [DLR]) space mission, proposes an active measurement approach to retrieve XCH4.

MERLIN is based on an integrated path differential absorption nadir-viewing LIDAR (LIght Detecting And Ranging; Gerhard Ehret et al., 2017; Kiemle et al., 2011, 2014; Pierangelo et al., 2015). MERLIN is scheduled for launch in 2023 (Gerhard Ehret et al., 2017). The integrated path differential absorption technique relies on differential absorption LIDAR measurements using a pulsed laser emitting at two wavelengths around the methane doublet at 1.645 μm, one wavelength accurately locked on a spectral feature of the methane absorption line, and the other wavelength, almost free from absorption, used as reference (Gerhard Ehret et al., 2017). The system specification for upper bound of the random error is 27 ppb (for a 50-km aggregation of shot-by-shot measurements along the satellite track). This active method enables measurements for all seasons, at all latitudes, for both daytime and night-time, while in the differential approach, the small size of the laser spot (~120 m at the surface along the track), the short length of the laser pulses, and the short interpulse period are expected to guarantee low systematic errors (target <3.7 ppb) with almost no contamination by water vapor and aerosols. Because the laser light is emitted as a very short pulse (typically 20 ns) and the received backscattered signal is recorded temporally, the hard target echo can be clearly separated from the light scattered by aerosols. MERLIN observations will be assimilated by atmospheric inversion systems to constrain methane surface emissions. A complete description of the MERLIN mission can be found in (Gerhard Ehret et al., 2017).

Based on inversion systems, Observing System Simulation Experiments (OSSE) have been conducted to study the impact on GHG surface emissions of uncorrelated random measurement errors (Chevallier et al., 2009; Houweling et al., 2004; Hungershoefer et al., 2010), of correlated random measurement errors (Chevallier, 2007), of systematic measurement errors (Chevallier et al., 2007), or of transport model errors as a whole (Chevallier et al., 2010; Houweling et al., 2010). Focusing only on the random part of the errors provides a too optimistic view of the performances of the tested observing networks to constrain surface emissions. Indeed, uncorrelated random errors statistically diminish with the time accumulation of raw satellite data (e.g., 3 Hz for SCIAMACHY, 0.25 Hz for GOSAT, and 20 Hz for MERLIN). On the contrary, systematic errors remain when accumulating data, and ultimately limit the exploitation of satellite data to constrain surface emissions.

In this paper, based on an original OSSE system that carries both random and systematic errors and on a detailed analysis of the plausible causes or these errors along the processing chain, we propose the first assessment of the potential impact of the MERLIN mission to improve knowledge on methane emissions from regional to global scale. The impact of MERLIN data on methane sinks is not addressed in this paper. Section 2 summarizes the OSSE system used. Section 3 presents the methodology employed to derive MERLIN random and systematic error scenarios on XCH$_4$ and the simulations performed. In order to make a comparison with an existing mission, section 3 also develops error scenarios for the GOSAT mission. Section 3 is supported by supporting information Text S1. Section 4 presents and discusses the results obtained in terms of uncertainty reduction for methane emissions assimilating MERLIN data, together with a comparison with GOSAT.

2. Inversion Frameworks

In this paper, we conduct a series of OSSE using inverse frameworks integrating error statistics on errors for future satellite retrievals and prior emissions and sinks, and two different transport models (see supporting information Text S1).

In brief, posterior error statistics for the CH$_4$ surface fluxes are computed, given (i) the sensitivity of the atmospheric CH$_4$ concentrations to the CH$_4$ surface fluxes (**H**), (ii) the a priori error statistics (**B**) on the CH$_4$ surface fluxes, and (iii) the statistics on the observation errors **R** (i.e., the measurement errors and errors related to the chemistry transport model used to compute the sensitivity of concentrations to the surface fluxes). The posterior error covariance matrix (or analysis) **A**, in a Bayesian framework, is expressed as

$$\mathbf{A} = \left[\mathbf{H^t R^{-1} H + B^{-1}}\right]^{-1} \tag{1}$$

with the assumption that the prior uncertainties observation errors, and consequently the posterior uncertainties, follow Gaussian distribution statistics and are unbiased (i.e., with zero mean). According to equation (1), posterior error statistics do not depend on methane mixing ratios. It is therefore possible to assess
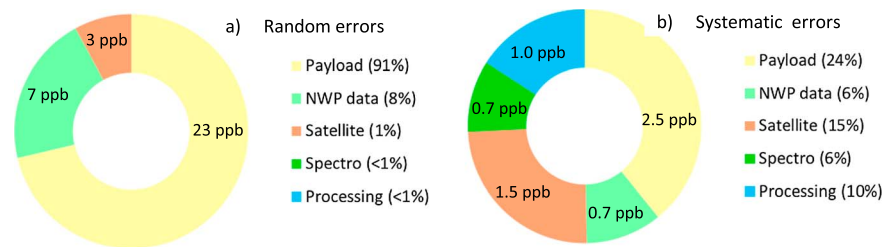
Figure 1. Relative share of contributors to the random error (a) and to the systematic error (b) for MERLIN XCH$_4$. Note that the representation is linear (parts per billion in the pies), while the actual summation of contributors is quadratic (percentages in the legend). NWP = the Numerical Weather Prediction data used to perform the level 2 retrievals; Spectro = spectroscopy; MERLIN = MEthane Remote LIdar missioN.

the impact of any existing or future observing system without actual measurement data as long as their location, their precision, and the precision of prior emissions in equation (1) can be estimated. An important limitation of such an approach is that observations and emissions are assumed to be unbiased, which has not been the case so far for satellite data (Buchwitz et al., 2016) in particular because of aerosol interference. Here the capability to convert an observation systematic error into an emission systematic error has been implemented, which is original considering most previous OSSE analyses (e.g., Wecht et al., 2014). The impact of observation systematic error β_y is a systematic error β_x on the surface fluxes that can be expressed as (see supporting information Text S1 for the derivation)

$$\beta_x = \mathbf{A}\mathbf{H}^t\mathbf{R}^{-1}\beta_y \tag{2}$$

Two inversion frameworks have been used in this paper, one from France (hereafter referred to as SIMGHG) and one from Germany (hereafter referred as MPI-Jena), differing by the transport model used and the inversion technique and setup implemented. Their description can be found in supporting information Text S1.

3. Error Scenarios on XCH$_4$ for MERLIN and GOSAT

3.1. General View

The assessment of the uncertainty reduction on methane emissions obtained from MERLIN data simulations requires performing a rigorous error analysis, from the MERLIN signals (level 0 data; see Gerhard Ehret et al., 2017) to the XCH$_4$ retrievals (level 2 data). At this early stage of the mission, the ongoing development of the processing chain does not allow using it for a complete error estimate. Therefore, we perform here an analysis based on a preliminary estimate of the different causes of errors and on some hypotheses on their spatiotemporal distribution. Errors statistics shall include random and systematic errors. We define the random errors as the uncorrelated (or high-frequency) part of the errors and the systematic errors as the low-frequency varying part, spatially and/or temporally correlated. The threshold between low and high corresponds typically to a few seconds time duration, for a satellite speed of typically 7 km/s (MERLIN case). By our restrictive definition, the random error is strictly noncorrelated between two measurements.

In the following, for both random and systematic errors, we estimate errors due to the payload, to the Numerical Weather Prediction (NWP) data used for the retrieval of XCH$_4$, to the spectroscopy, to the satellite, and to the data processing (Figure 1). Errors of these different components are estimated and spatially and temporally distributed on geophysical variables: surface reflectivity, aerosol optical depth (AOD), and surface pressure for random errors; and latitude, albedo, aerosol transmission, surface pressure, topography, and season for systematic errors. This analysis (section 3.2) is detailed below and leads us to define scenarios of random and systematic errors for MERLIN XCH$_4$ that are then applied to the atmospheric inversion systems. The outcome is an estimate of the residual uncertainty on methane emissions when assimilating MERLIN (level 4 data; see sections 2 and 4). We also develop scenarios of uncertainty for GOSAT mission (section 3.3) in order to compare GOSAT and MERLIN performances for uncertainty reduction on methane emissions.

3.2. MERLIN Error Statistics

3.2.1. Random Errors

We define random observation errors as all random errors related to the inability of the model to represent the observations (**R** matrix in equation (1), Rodgers, 2000). It should include the measurement error on XCH$_4$, the transport model error, and the aggregation error.

3.2.1.1. Measurement Errors

For the measurement error, the potential causes of random error include the payload, the NWP data used for the retrieval of level 2 MERLIN product, the platform, the spectroscopy, and the data processing. This part of the error reduces in when aggregating measurements. The instrument noise contributors are such that this reduction remains valid up to 50 km, the typical aggregation length chosen here, the speckle noise, for instance, being negligible. As detailed in the supporting information Text S2 and summarized in Figure 1a, the dominant (~3/4) cause of random error for MERLIN XCH$_4$ comes from the payload and more precisely from the measured DAOD (differential absorption optical depth), using a commercially available avalanche photo diode that does not require extra cooling as the detector unit. The individual noise terms of such an avalanche photo diode device and how these terms contribute to the overall radiometric resolution can be found in (G. Ehret et al., 2008, Eqs. 7 to 11). For the calculation of the radiometric performance, we used equation (S2d) which is a more compact version provided by the payload supplier. XCH$_4$ is linked to DAOD by the following relationship:

$$XCH_4 = \frac{DAOD}{\int_{P_{surf}}^{0} WF \, dP} \qquad (3)$$

where WF is the MERLIN specific weighting function (Gerhard Ehret et al., 2017). Other minor causes of random errors for XCH$_4$ come from the vertical weighting function WF and include the impact of spectroscopy, of external NWP data (temperature, surface pressure, and humidity, necessary in the retrieval procedure of XCH$_4$), and of estimations of the target scattering surface elevation. They appear however negligible when quadratically summed up with the payload errors. As the processing of MERLIN data up to level 2 can be written in a fully analytical form, the error budget for XCH$_4$ is estimated mostly through an analytical approach (see supporting information Text S2). XCH$_4$ errors have been calculated and tabulated once for all for a 50-km aggregation along the satellite track as a function of the parameters determining the analytical expression of XCH$_4$ errors (see equations (S2a)–(S2h) in the supporting information Text S2): surface reflectivity (assumed to be reflectance/π, calculated from 0.01 to 0.4 by steps of 0.01), AOD (from 0 to 0.5 by steps of 0.1), and surface pressure (from 500 to 1050 hPa by steps of 50 hPa.

From these random error causes for MERLIN observations, we have developed one scenario of random measurement error for MERLIN to be used in the OSSE system (see Text S2 for details). The nominal random measurement error for MERLIN for a clear-sky optimal scene of surface reflectivity 0.1 sr^{-1} and 50-km averaging is found at ±22 ppb, compliant with the system specification requirements (±27 ppb). However, random errors for other scenes (i.e., with different values of surface reflectivity or AOD) are generally larger than this reference situation, and for MERLIN they range from 18 to 93 ppb (respectively 5th and 95th percentiles of the distribution), with a minimum of 6 ppb, a 68th percentile of 47 ppb, and a mean of 42 ppb.

3.2.1.2. Transport and Aggregation Errors

The transport model error has been estimated from two simulations performed with LMDZ, using two different convection schemes, following either Tiedtke (1989) or Emanuel (1991). This approach has been chosen as parametrizations of the vertical transport are one of the main causes of errors in modeled transport (Locatelli et al., 2015). Monthly averaged methane columns from the two LMDZ simulations have been subtracted and used to represent the spatiotemporal patterns of the model error. The magnitude of the model error is obtained by scaling these monthly differences between 8 and 23 ppb in order to have similar variations as the error statistics obtained in Cressot et al. (2014) using a different but more comprehensive approach to estimate the magnitude of model errors. We assume here that this range includes aggregation errors as well. The transport model error defined that way show quite strong spatial gradients, especially between the two hemispheres, and a pronounced temporal variability. The model error is added on top of previous random errors and is not reduced by the square root of the number of measurements.
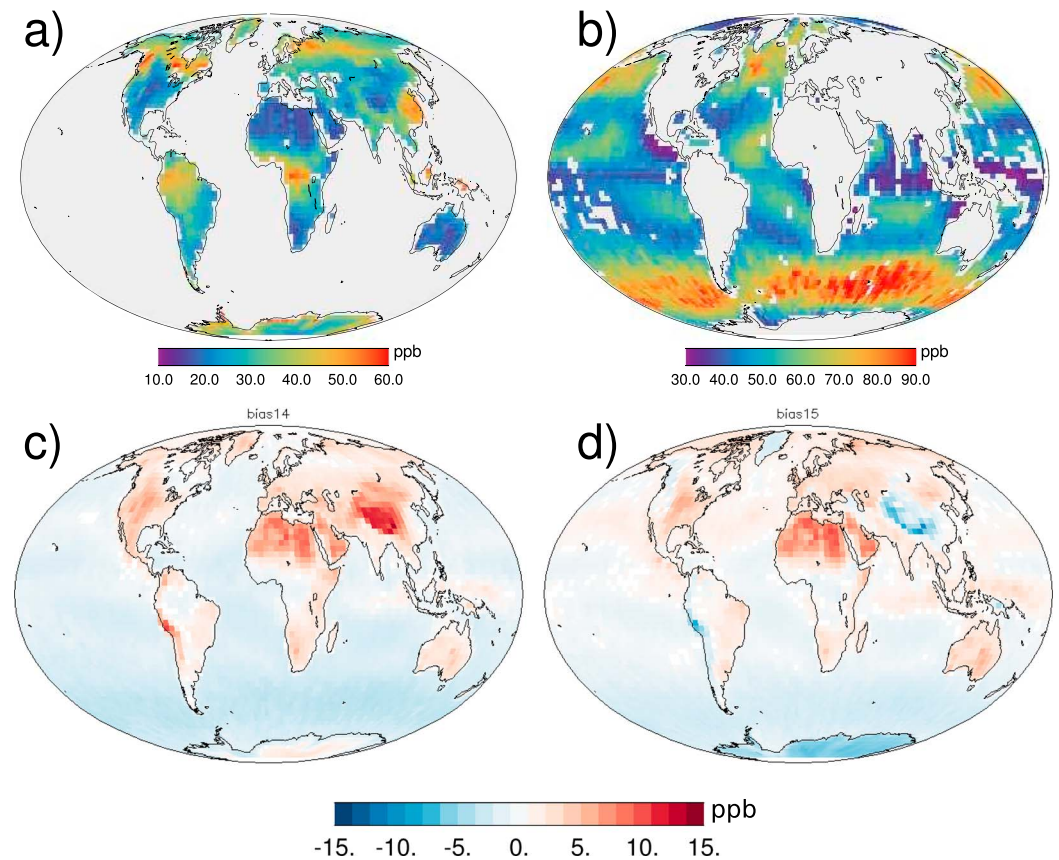
Figure 2. (a, b) Yearly average at 50 km of MERLIN random error for the methane atmospheric columns (ppb) for each LMDZ grid cell over continental regions (a) and over oceanic regions (b). Color scales are different between the two maps reflecting larger random errors over the oceans. (c, d) Two examples of scenarios for MERLIN systematic errors (ppb) with identical (c) or opposed signs (d) when combining albedo and surface pressure. All scenarios are presented in Figure S4b. MERLIN = MEthane Remote LIdar missioN.

3.2.1.3. Total Random Error

The spatial breakdown of the total random observation error (measurement + model) are shown in Figure 2a for continents and Figure 2b for oceans. Total random observation errors range from 16 to 60 ppb over land and from 22 to 105 ppb over oceans (5th and 95th percentiles), with larger errors over oceans as compared to continents, which is mostly explained by the decrease of the XCH_4 errors with the surface reflectivity (higher for land than for ocean). The highest error values can be related to cloud covers limiting the number of clear-sky observations (e.g., equatorial continents), to reflectance effects (e.g., southern oceans or snow surfaces that have lower reflectivity than soil/vegetation surfaces at the MERLIN wavelength, such as Canada or Siberia), to aerosol presence (e.g., tropical Atlantic) or to transport errors (e.g., Asia, tropical continents, and Siberia). Figure 2 looks very similar to the first estimate of MERLIN precisions made by Kiemle et al. (2014; see their Figure 5) using a composite database of Cloud-Aerosol Lidar and Infrared Pathfinder Satellite Observation cloud/aerosol optical depths and Moderate Resolution Imaging Spectroradiometer/Global Modeling and Assimilation Office reflectances for year 2007. The maps of Figure 2 are used to fill the diagonal (variances) of the **R** matrix of equations (1) and (2). The total number of MERLIN data aggregated over 1 year is about 1,600,000 (650,000 over lands).

3.2.2. Systematic Errors

Following our definition, systematic errors consist in spatially and/or temporally correlated errors. For instance, an error that would depend on surface pressure is spatially correlated because of the relatively smooth patterns of surface variations on certain areas (plains, oceans …). Consequently, their impact in terms of fluxes error strongly depends on their spatial and temporal distribution. In the following, a systematic error of *y* ppb is to be interpreted such that 68% of the data are in the range ±*y* ppb around the mean value of the

Table 1
Contributors to Systematic Errors, Their Amplitude, Their Root Cause, the Associated Geographical Pattern, and Their Dependency Mathematical Relation

Level 2 systematic error contributor	Relative systematic error (RSE)	Potential root cause	Geographical pattern	Dependency relation
DAOD calibration path variations between *on* and *off*	0,084%	Thermoelastic effects inside the instrument	Latitude (50%)/season (50%)	Sine/sine
DAOD linearity residuals	0.099%	Variation of the received flux on the detector chain	Reflectivity × aerosol transmission	Linear
Surface pressure (NWP)	0.024%	Regional errors in NWP models	Regional	
Scattering surface elevation	0.059%	Errors on satellite altitude after orbit restitution	Latitude	Sine
Temperature (NWP)	0.028%	Latitudinal and/or regional errors in NWP models	Latitude	Sine
Spectroscopy model knowledge	0.035%	Limited knowledge of spectroscopy model; its impact depends on pressure and also on temperature	Surface pressure	Linear
Processing (averaging of data)	0.056%	Averaging along 50 km and associated bias correction	Topography (25%) reflectivity/aerosol (75%)	Linked to SP changes/Linear
Constant error on DAOD	0.03%	Constant error on DAOD gives variable error on XCH_4	Surface pressure	Linear
Total (quadratic)	0.164%			
Total in ppb	2.926			

Note. A detailed analysis is provided in supporting information Texts S2 and S3. SP = surface pressure; DAOD = differential absorption optical depth; NWP = Numerical Weather Prediction.

error. This corresponds to one sigma convention for a Gaussian distribution but may be easily extended to non-Gaussian distributions. The constant part of the error is removed in the assimilation process through the optimization of a global offset. Here we ignore model error correlations (off diagonal term of the **R** matrix in equation (1), as in most OSSE.

Several possible causes of systematic errors have been identified for MERLIN (Ehret et al., 2017): from the payload, the DAOD calibration variations between *on* and *off* wavelengths (thermoelastic effects inside the instrument) and linearity issues (variation of the received flux leading to a nonlinear detector response). The requirement for the relative online/off-line calibration stability is ~8.10−4 in order to meet the error budget given in the second column of Table 1. The envisaged calibration concept described in Ehret et al. (2017) has been studied in detail in the laboratory and was applied by the MERLIN airborne demonstrator named CHARM-F where a calibration stability of about 1 part to the 10^4 could be demonstrated using the Allen variance method (Fix et al., 2015). A similar data analysis will be used in the ground processing to analyze the calibration stability of the MERLIN measurements in orbit. The XCH_4 error due to the detector nonlinearity will be characterized on ground with an accuracy better than 0.1% which corresponds to a nonlinearity error of similar amount. For quantification of a possible detector degradation on orbit, we will use the long-term monitoring function for comparing two pairs of online/off-line measurements over regions with high reflectivity (deserts) to those from regions with low reflectivity (water or snow). The spectral control (frequency jitter, spectral purity, etc.) of the online and off-line wavelengths will be performed by a dedicated frequency reference unit which is part of the payload subsystem as described in Ehret et al. (2017). Note that an independent and very sensitive monitor of the spectral purity on orbit is given from a comparison of the lidar echoes at different optical depth. For this, the cloud echoes which provide significantly reduced DAOD values will be compared to the ground returns. Other possible causes of error regarding the payload include constant error on DAOD converting into variable error on XCH_4, temperature or pressure errors from NWP models, errors on satellite altitude after orbit restitution, limited knowledge in the spectroscopy model, and data processing (averaging at 50 km along the track).

The representation of atmospheric transport can also cause systematic errors. The assimilation of atmospheric columns limits the impact of the usual underestimation of synoptic variability at the surface of coarse global models (Geels et al., 2007). However, most global models underestimate the sharp methane gradient in the stratosphere with possible latitudinal differences, which can lead systematic errors (Patra et al., 2011).

Table 2
Weight Attributed to the Individual Systematic Error Patterns to Get the Mixed Scenarios

Pattern	Amplitude of the relative systematic error	In ppb
Seasonal	0.059%	1.057
Latitude	0.088%	1.575
Albedo*Tatm	0.141%	2.510
Regional	0.024%	0.427
Surface pressure	0.046%	0.821
Topography	0.014%	0.250
Total (quadratic)	0.164%	2.926

Note. The same convention as for the random error applies here: The value given here in parts per billion (ppb) corresponds to the value such that 68% of the histogram has an absolute value error below.

We do not address this issue explicitly but assume here a possible latitudinal dependency of the nonuniform contribution of such an error (Tables 1 and 2).

Based on the expertise at CNES and DLR, the individual systematic errors have been estimated and distributed spatially and temporally on geophysical variables (Table 1): latitude, surface pressure, topography, albedo (reflectivity), AOD, and seasons (see supporting information Text S2 and Figure S4a). For instance, thermoelastic effects have been distributed 50% in latitude (short-term effects) and 50% on seasons (long-term effects). Processing effects have been distributed according to topography, albedo, and AOD. The total value in Table 1 (~ 2.9 ppb), in parts per billion, corresponds to the best estimation of total systematic error at this point of the mission. It is important to notice that, at this stage, it complies with the objective to keep total systematic error below 3.7 ppb. Once all causes of systematic errors are distributed, we merge the contributors having the same patterns to get a view of the systematic error per pattern type (Table 2). Overall, the main patterns contributing (quadratic sum) to the 2.9 ppb total systematic error is albedo (2.5 ppb) followed by latitude (1.6 ppb), seasons (1.1 ppb), and surface pressure (0.8 ppb).

Table 2 is not sufficient to get a mixed error global distribution, because the question still holds on how to account for the sign (positive or negative) when combining the individual patterns of systematic errors. Therefore, a statistical approach is chosen to perform the combination, in which total monthly systematic error maps are generated for all possible sign combinations of the five different spatial and temporal patterns of Table 2 (seasons, latitude, albedo × transmission, surface pressure, and topography) when multiplying each weighted pattern by +1 or −1. Doing so, 32 scenarios ($2^5 = 32$) of possible total systematic errors have been generated for MERLIN (Figure S4b) to be used as inputs for the OSSE (equation (2), β_y vectors). Each map is scaled such that 68% of the distribution is at 2.9 ppb. An illustration of the spatial distribution of two error scenarios is provided in Figures 2c and 2d.

In reality, the residual systematic error patterns (after correction of identified biases) will be unknown. The distribution of systematic errors generated here aims to be statistically representative and conservative regarding error distributions but does not claim to be the actual distribution.

3.3. GOSAT Error Statistics

We have compared the expected MERLIN performances with GOSAT ones. To do so, for GOSAT, we use the SRPR product, version 2.3.7, of ESA's Climate Change Initiative (http://www.esa-ghg-cci.org/) for GOSAT (Butz et al., 2010). SRPR, produced by SRON (*Netherlands* Institute for Space Research), includes a best uncertainty description attached to each XCH$_4$ data. This uncertainty corresponds to the Bayesian estimate of the measurement uncertainty that is degraded (R. Detmers, personal communication, October 2016) to account for the comparison with data from the Total Carbon Column Observing Network (Wunch et al., 2011). We use these modified values (factor ~1.5 increase) to represent the random error of GOSAT data (not shown). GOSAT random error ranges from 14 to 29 ppb, (respectively 5th and 95th percentiles), with 68% of the data within ±20 ppb (mean of 19 ppb), about 3 times lower on average than the MERLIN random errors at 50-km resolution. However, the total number of GOSAT data aggregated over 1 year is about 280,000, only 20% of the number of MERLIN data. The SRPR product includes bias-corrected XCH$_4$ and the bias correction applied by the SRON team to the raw data. Once centered, the bias correction field appears to have a ±2.6 ppb spread (at 68%), which makes our scenario S1 for GOSAT.

Bias-corrected SRON data still contain systematic errors, which have been estimated in the range [4.6–6.3] ppb by comparison with Total Carbon Column Observing Network data (Buchwitz et al., 2016). The patterns of these residual systematic errors are largely unknown, but the usual suspects for such a passive measurement as performed by GOSAT are aerosols, water vapor, and thin clouds (S. Houweling, personal communication, October 2016). We therefore distribute the residual systematic errors of GOSAT on the distribution of these geophysical parameters. Aerosols are derived from Moderate Resolution Imaging Spectroradiometer climatology products (Frey et al., 2008; Remer et al.,

2005); water vapor fields come from European Centre for Medium-Range Weather Forecasts ERA-Interim re-analysis (Dee et al., 2011); thin clouds are identified from the CALIOP_05 km CLay cloud mask (O'Dell et al., 2017) as clouds having a value of the integrated attenuated backscatter below 0.001. In addition, similar to MERLIN, a bias dependent on latitude is taken into account for GOSAT, linked to possible transport model errors (see section 3.2.2), but also to stratospheric aerosol (O'Dell et al., 2017). We then combine Scenario S1 with each of these geophysical biases to get a total systematic error pattern for GOSAT. Again, as for MERLIN systematic errors, the sign of each contributor is uncertain and we therefore generate all possible scenarios by multiplying each individual pattern by +1 or −1. Doing so, we obtain 32 scenarios of total systematic error for GOSAT (Figure S4c) to be used as inputs for equation (2) (β_y vectors). Lacking more precise information, weighting coefficients have been arbitrarily defined for each pattern: it is unity for the SRON retrieval bias and 0.25 for each of the four geophysical biases. The total bias for each scenario is further scaled to get a spread at 68% of ±5.45 ppb, which corresponds to the mean of the residual error (between 4.6 and 6.3 ppb) estimated in (Buchwitz et al., 2016).

About the GOSAT/MERLIN comparison, one could argue that the known bias correction for GOSAT should be applied to correct GOSAT data. We did not do so to make a fair comparison with MERLIN for which we do not know at this stage what part of the systematic errors will be possibly corrected, when actual data are there. Also, a more physically based analysis of MERLIN systematic errors in the future, using the instrument simulator currently under development, will allow realistic scenarios among the 32 generated (Figure S4b). This may reduce the impact of systematic errors if amplifying scenarios can be discarded based on physical arguments. For this reason, the systematic errors estimated here are probably conservative.

3.4. Simulations and Diagnostics

The error scenarios developed to represent MERLIN and GOSAT random and systematic errors have been run in the SIMGHG flux simulator. For the two satellites, each scenario is converted into geographically distributed errors on methane emissions using the SIMGHG simulator (β_x from equation (2), which also provides the residual random error (σ_{random}) from the diagonal of **A** matrix from equation (1). Assuming their independence, β_x and σ_{random} errors are quadratically combined to generate the total residual error on methane emissions after inversion for each scenario (root-mean-square [RMS] in mg $CH_4 \cdot m^{-2} \cdot day^{-1}$). Finally, this total residual error $\sqrt{\sigma_{random}^2 + \beta_x^2}$ is converted into uncertainty reduction (E_{red} in percent) as compared to the prior (random only) error on surface fluxes (σ_{prior}) following equation (4):

$$E_{red} = \left(1 - \frac{\sqrt{\sigma_{random}^2 + \beta_x^2}}{\sigma_{prior}} \right) * 100 \qquad (4)$$

Under the Bayesian theory, the higher the information content brought by the assimilated data is, the lower σ_{random} is compared to σ_{prior}. However, the introduction of systematic errors (β_x) can cause the overall uncertainty on the posterior emissions ($\sqrt{\sigma_{random}^2 + \beta_x^2}$) to be higher than σ_{prior}, which implies a negative error reduction with our formalism ($E_{red} < 0$). If biased data could be identified, they would be discarded from the inversion and, in this case, the uncertainty reduction would remain positive or null. However, in the real world, biased data are not always identified, which justifies to keep the negative values of E_{red} as indicators of regions where unknown systematic errors could degrade knowledge on surface emissions (e.g., Chevallier et al., 2007).

SIMGHG solves the inversion problem for 254 continental regions. It is also possible to aggregate the calculated variances and covariances for each SIMGHG region and each week (from equations (1) and (2) into larger regions (e.g., Europe, Tropical Asia, …), following the region map of the Tracer Transport Model Intercomparison Project (TransCom, Gurney et al., 2004) and on a yearly basis, in order to get annual error budgets for broader regions or at global scale. In the next section, we present both uncertainty reductions (%) and residual errors per large region (Tg CH_4/year) for the ensemble of scenarios described in this section.
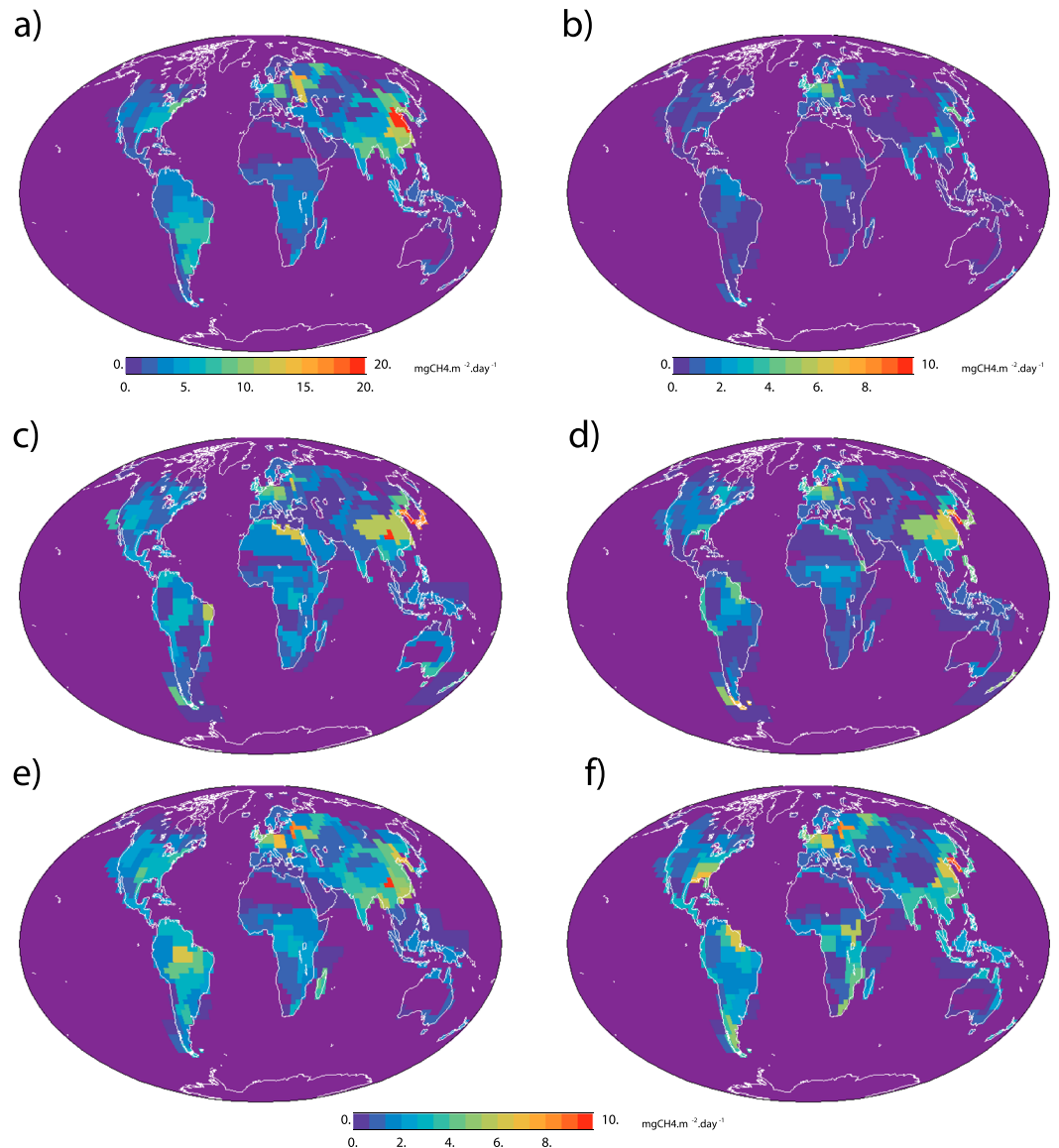
Figure 3. Errors on methane emissions (mg $CH_4 \cdot m^{-2} \cdot day^{-1}$. (a) The prior random errors as injected in the OSSE (σ_{prior}, B matrix, see section 3.2.1). (b) The residual random error σ_{random} as estimated by the OSSE. Maps (c) to (e) represent the total residual errors $\sqrt{\sigma_{random}^2 + \beta_x^2}$ dominated by β_x for MERLIN scenario 14 (see section 3.2.2) in different configurations: All MERLIN data are assimilated (c), only MERLIN data over land are assimilated (d), and only MERLIN data over oceans are assimilated (e). (f) The residual systematic errors β_x for GOSAT scenario 14 (see section 3.3). MERLIN = MEthane Remote LIdar missioN; OSSE = Observing System Simulation Experiments; GOSAT = Greenhouse Gases Observing SATellite.

4. Results and Discussion

4.1. Uncertainties at Regional Scale

Solving for equations (1) and (2) leads to random and systematic uncertainties on methane emissions that can be quadratically combined into the total residual error. The random part of the residual uncertainty (σ_{random}, Figure 3b) shows smaller values than the prior estimate (Figure 3a) for all continental and oceanic regions as, mathematically from equation (1), σ_{random} is smaller or equal to σ_{prior} (Rodgers, 2000). The smaller σ_{random}, the larger the constraints brought by the MERLIN data. The difference between σ_{random} and σ_{prior} is especially visible on continental regions (e.g., tropics or midlatitudes). The systematic part of the residual uncertainty (β_x) shows more contrasted results, with most continental regions showing smaller uncertainties than σ_{prior} but with some continental regions and most oceanic regions showing comparable to larger
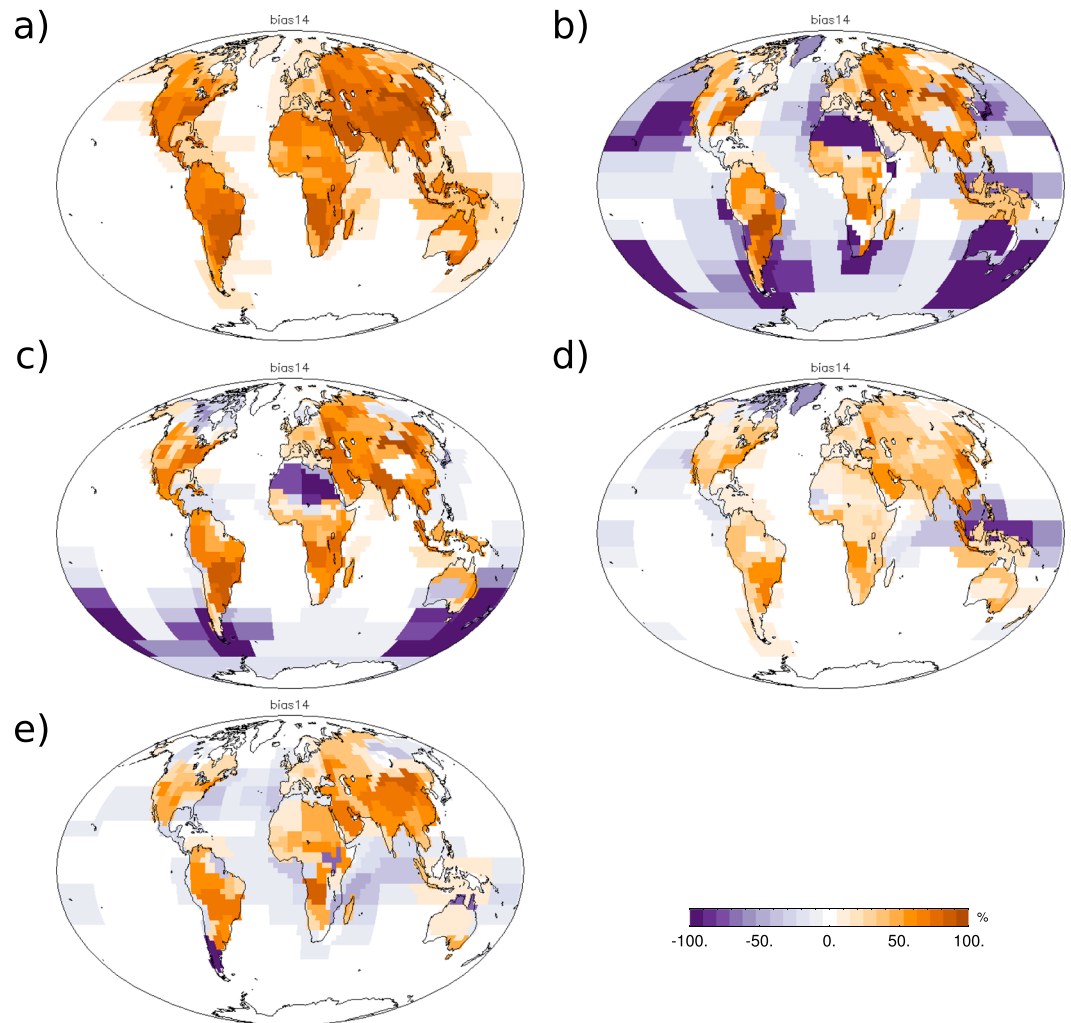
Figure 4. Example of uncertainty reduction E_{red} (%; see equation (4)) on methane emissions when only random errors are taken into account (a) and for the same three configurations of systematic error scenario 14 as shown in Figure 3 (b, c, d). (b) All MERLIN data are assimilated. (c) Only MERLIN data over land are assimilated. (d) Only MERLIN data over oceans are assimilated. (e) All GOSAT data are assimilated. A negative uncertainty reduction indicates regions where systematic errors lead to larger uncertainties than the current uncertainty on surface emissions. Contributions of the different regions to the global methane emissions are shown in Figure 7 and printed in Table 3. Residual uncertainties on emissions for all scenarios are presented in Figures S4d (MERLIN) and S4e (GOSAT). MERLIN = MEthane Remote LIdar missioN; GOSAT = Greenhouse Gases Observing SATellite.

uncertainties compared to σ_{prior}. Figure 3c illustrates this for scenario 14 (all scenarios are visible in Figure S4d). Differences remain small and not visible for ocean regions in Figure 3 because methane emissions and their uncertainties are small over ocean regions (global uncertainty of 4 Tg/year only). Using only data over land (Figure 3c) or oceans (Figure 3d) leads to similar total residual errors as with all data. However, regional changes in the magnitude of residual uncertainties can be observed in Figure 3, with some regions even presenting smaller residual uncertainties (e.g., deserts). In order to analyze more precisely the differences between these configurations, we now present the uncertainty reductions calculated from equation (4).

At the scale of the regions inverted by the SIMGHG simulator, Figure 4a shows the spatial pattern of the uncertainty reductions on CH_4 emissions when only accounting for MERLIN random errors. Unsurprisingly, when removing systematic errors, uncertainty reductions are excellent over land (range 40–80%) and significant above coastal ocean regions (range 0–30%). When including the effect of systematic errors (Figure 4b, example of scenario 14, see supporting information Figure S4d), most continental regions still show positive, but generally smaller, uncertainty reduction indicating that MERLIN data bring information there. However,

most oceanic regions and deserts show negative error reductions (bluish colors in Figure 4b). As could be expected, systematic errors dominate the residual error budget and can significantly degrade uncertainty reductions to smaller positive values (~ most continental regions) or even to negative values (~ oceans and deserts). This negative result has to be moderated by the fact that oceans and deserts represent only 3% at most of global methane emissions (Saunois et al., 2016). In our approach, such low emissions are associated to a very small prior uncertainty (σ_{prior}, Figure 3a), therefore enhancing the relative impact of systematic errors on uncertainty reductions. Our choice to distribute one part of the systematic error proportional to the surface albedo is the main cause of such large negative values. Whether such choice is physically realistic or not cannot be assessed at present.

Overall, the mean uncertainty reduction for MERLIN is +32% (range −1%/+65%) for continental regions and −200% (range −400%/−100%) for oceanic regions. These estimates account for the spatial and temporal error correlations between emitting regions (off diagonal terms of the A matrix in equation (1). Removing Sahara and central Australia from the residual error budget increases the global mean uncertainty reduction at the scale of the regions used in the inversion from 32% to 60% (range +29%/+92%).

The combination of individual components of the systematic errors can also penalize the uncertainty reduction. This is the case for most ocean regions (e.g., North and South Pacific and North Atlantic) when albedo effects have the same sign in the combination as surface pressure effects (scenarios 1, 2, 7–10, 15–18, 23–26, 31, and 32). When albedo effects have opposite sign as surface pressure effects (other scenarios), the ocean/continent contrast is enhanced and brings contradictory information to coastal land and ocean regions, especially when strong western winds link these regions through atmospheric transport (e.g., south of South America, Coastal regions of Australia, or boreal north America). Such situations degrade the constraints brought by the data and lead to negative uncertainty reductions. Again, when more physical models of MERLIN are available, it should be possible to determine whether such combinations are physical or not.

The way systematic errors are prescribed here can generate large ocean/land contrasts. In order to evaluate the impact of this approach, we have performed simulations assimilating only land data or only ocean data. When only assimilating MERLIN data over continents, uncertainty reductions show less negative values over open oceans and coastal zones, with the exception of southern oceans where only few data are assimilated in this case (Figure 4c). The uncertainty reductions achieved in this case for continental regions are of the same order, albeit smaller (deserts removed), than with all data (~ +42%, with values ranging between −19% and 89%) with similar zones of negative values. Oceanic regions still show a degradation although slightly less pronounced than with all data. When only assimilating MERLIN data over oceans, areas with positive uncertainty reductions remain over land, albeit generally smaller for individual regions (Figure 4d). Negative values largely disappear, implying a better global performance. This result may be explained by the smoother structure of systematic errors above oceans compared to above continents (see supporting information Figure S4a), by the suppression of the longitudinal gradient of the systematic error over coastline regions and by the smoothing of continental signals when transported from (mostly continental) emission zones to remote oceanic data locations. However, here error correlations caused by transport model uncertainty are only indirectly accounted for as a latitudinal dependency (section 3.2.2): Taking their longitudinal part into account would likely degrade this configuration because of systematic errors in the representation of methane plumes far from their emission location over land.

4.2. Annual Residual Errors at Continental Scale

The total residual uncertainty on methane emissions calculated from SIMGHG inversions are now aggregated onto the 11 continental regions defined in the TRANSCOM experiment (Gurney et al., 2004) for MERLIN error scenarios, allowing a more synthetic analysis at a larger scale than the previous smaller regions. Error correlations are taken into account when doing both spatial and temporal aggregations. For each TRANSCOM region, a boxplot represents the results of all scenarios for systematic errors on CH_4 emissions (bias) as well as for the total residual error (RMS, corresponding to $\sqrt{\sigma_{random}^2 + \beta_x^2}$). They are compared to the corresponding prior and posterior (random) errors. Large desert areas in Northern Africa and Australia have been removed from the analysis because these regions have null or very low methane emissions but, under our assumptions, contribute strongly to systematic errors through the chosen albedo dependency of the systematic errors (cf. section 4.1 and Figure 4b).
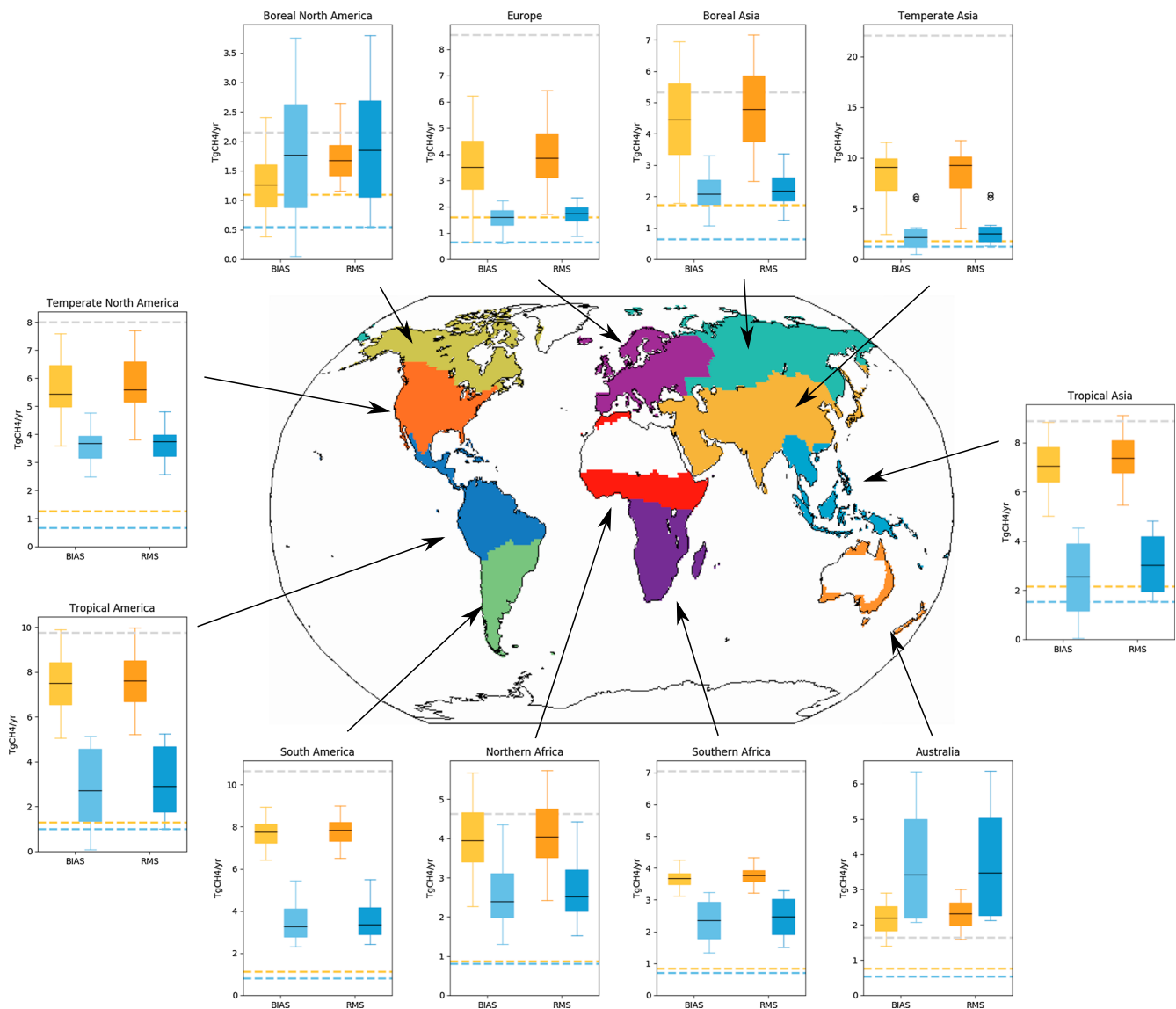
Figure 5. Posterior error statistics of regional methane emissions for MERLIN and GOSAT (Tg CH$_4$/year) using SIMGHG. For 11 continental regions, a comparison between residual errors on methane emissions between MERLIN (blue) and GOSAT (orange) is proposed: Dark blue/orange boxplots (the two rightmost boxplots of each region) represent the MERLIN/GOSAT residual total error (RMS), light blue/orange boxplots (the two leftmost boxplots of each region) represent the MERLIN/GOSAT residual systematic error, and dashed blue/orange lines are the MERLIN/GOSAT residual random error. The prior error is shown as the dashed gray lines. The box extends from the lower to upper quartile values of the data, with the median values shown in black; the whiskers show the range of the data between the first and third quartiles ±1.5 times the interquartile range. White continental areas correspond to desert zones of Australia and Sahara that have been removed from the analysis (see text). MERLIN = MEthane Remote LIdar missioN; GOSAT = Greenhouse Gases Observing SATellite; RMS = root-mean-square; SIMGHG = OSSE system based on LMDZ model (see section 2).

At this spatial scale, the residual random errors are small (average generally <2 Tg CH$_4$/year). The large number of observations assimilated allows the random part of the uncertainty to largely be decreased, although MERLIN expected random errors at a 50-km resolution are not the smallest of the existing or planned missions (Gerhard Ehret et al., 2017; Jacob et al., 2016). However, the contribution of random error on the total error budget remains limited, the latter being dominated by the impact of systematic errors for all regions, for all mean values per regions, and for most individual scenarios (Figure 5). This is visible with the boxplots of Figure 5 showing total residual uncertainties (RMS) which remain very close to boxplots accounting only for the systematic errors (BIAS). This result stresses again the importance of properly accounting for systematic errors and, whenever possible, correcting them, if one wants to robustly improve the estimation of methane emission estimates.

Table 3

Mean (Median) and Range of Uncertainty Reductions (%) on Methane Emissions Inferred by SIMGHG for 11 Regions Mapping all Continents for MERLIN (Left Columns), GOSAT (Central Columns), and for Cressot et al. (2014) (Right Columns)

Regions	MERLIN		GOSAT (this study)		GOSAT, (Cressot et al., 2014)	Fraction of global emissions (%)
	Mean (median)	Range	Mean (median)	Range	Mean	
Europe	80 (80)	73/90	54 (55)	25/80	18	5
Boreal Asia	58 (59)	37/77	10 (10)	−34/53	11	7
Temperate Asia	87 (88)	71/94	63 (58)	47/86	40	18
Tropical Asia	65 (66)	46/83	17 (17)	−2/39	30	20
Australia	−132 (−111)	−287/−30	−40 (−41)	−83/3	1	2
Northern Africa	42 (45)	4/67	11 (13)	−24/48	53	8
Southern Africa	66 (65)	53/79	47 (46)	39/54	13	8
Boreal North America	8 (14)	−76/75	19 (22)	−23/46	7	4
Temperate North America	54 (53)	40/68	28 (30)	4/53	18	7
Tropical America	68 (70)	46/90	22 (22)	−2/47	20	17
South America	66 (68)	48/77	27 (26)	15/39	30	3

Note. The rightmost column indicates the % of the global methane emissions due to the associated region. A negative uncertainty reduction indicates regions where systematic errors lead to larger uncertainties than the current uncertainty on surface emissions. By construction, Cressot et al. (2014) cannot have negative values. Sahara and Central Australia have been removed from the analysis (see text). Fractions of global emissions per region (last column) are estimated from Saunois et al. (2016). The missing 1% in the fraction of global emissions stands for oceanic emissions. MERLIN = MEthane Remote LIdar missioN; GOSAT = Greenhouse Gases Observing SATellite.

The median of residual biases ranges generally between 2 and 4 Tg CH_4/year at this subcontinental scale. For all regions but Australia and Boreal North America, the RMS of all scenarios are smaller than the initial (random only) error, indicating a clear improvement in the knowledge of methane emissions with MERLIN data, mostly thanks to the lower systematic errors compared to other missions.

In terms of uncertainty reduction for the 11 (continental) regions (Table 3), the values range from −132% (Australia) to +87% (temperate Asia). Only Australia shows negative error reductions, associated to low emissions and low prior uncertainty (see section 4.1). The largest uncertainty reductions are achieved for temperate regions and for tropical regions (Gerhard Ehret et al., 2017, see their Figure 7), with uncertainty reductions from 54% (temperate North America) to 87% (temperate Asia) for temperate regions and from 42% (northern Africa) to 68% (tropical America) for the tropics. Boreal regions also show significant uncertainty reduction from 8% (boreal North America) to 58% (boreal Asia).

For boreal North America, although the median RMS is below the prior error, some scenarios infer a degradation. The situation is worse for Australia with no scenario improving the prior error. Indeed, we identified in section 4.1 albedo and surface pressure and their relative sign in the error combination as the main cause limiting the uncertainty reductions for subregions inside boreal North America and Australia. The penalty is largest for Australia (negative uncertainty reduction) and more limited for boreal North America (small positive uncertainty reduction). Even when removing the desert areas of these two regions (white zones in Figure 5) the issue remains, as also possibly related with the coastal effect noticed in section 4.1.

Thanks to its active measurement technique, MERLIN is expected to improve our knowledge on methane emissions all around the world and all year round, including at high latitudes. The breakdown of TRANSCOM regions does not allow one to assess the impact of MERLIN data on Boreal regions as a whole because Europe is not separated into boreal and temperate regions. Therefore, we extracted a *boreal region* from the individual regions of section 4.1 to estimate the uncertainty reduction induced by MERLIN data (Figure 6). At this more latitudinal scale, and for all error scenarios, residual total errors for MERLIN are lower than the initial error, with an uncertainty reduction of about 50%, indicating a significant improvement of the knowledge on methane emissions for this important climate-sensitive zone (Figure 6).

4.3. Comparison With GOSAT

We now compare the expected performances of MERLIN with the estimated ones of GOSAT based on the error scenarios developed for this already flying satellite (section 3.3). At the scale of individual regions used in the OSSE, for all regions but deserts, GOSAT present comparable to larger residual errors than MERLIN (Figure 3f), indicating that MERLIN is generally reducing uncertainties on methane emissions more than
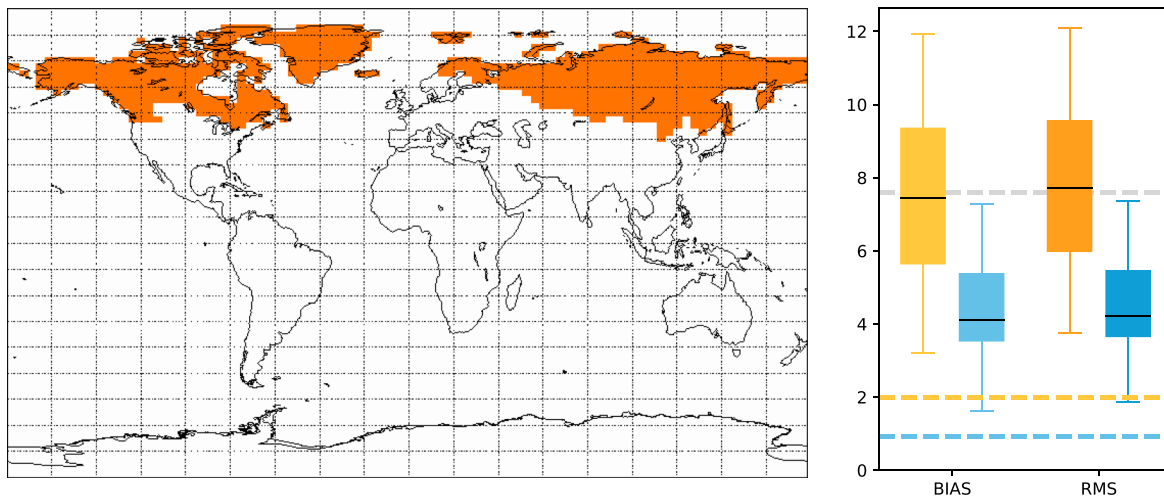
Figure 6. (left) Area (in red) of the model pixels used to define the boreal region. (right) Boxplot representing the residual error after inversion for the boreal region (same color code as in Figure 5).

GOSAT. More precisely, uncertainty reductions achieved by GOSAT for continental regions are 23% on average over all scenarios (ranging from −40% to 78%, example in Figure 4e for scenario 14). The smaller random errors prescribed for GOSAT as compared to MERLIN are more than compensated by larger average systematic errors for GOSAT (Figure S4e). Negative uncertainty reductions also appear for GOSAT but for different regions than for MERLIN, as a result of the spatial structure of the systematic errors prescribed for GOSAT (albedo, aerosols, water vapor, and thin clouds). In this case negative uncertainty reductions are found mainly for tropical oceans and continents, boreal North America and boreal North Asia, and the Sahara, mainly. The mean uncertainty reduction for GOSAT over the oceans is about −80% (−200% to 22%). This value, not as bad as the −200% found for MERLIN, is probably explained by the penalty imposed by the combined effects of surface albedo and surface pressure for MERLIN above oceans. However, large negative values (albeit smaller absolute values than for MERLIN) in coastal areas are also visible for GOSAT (Figure 4e) but appear less contrasted than for MERLIN, again linked to the spatial distribution of systematic errors but also to the fact that there are less GOSAT data over oceans (70,000 over oceans versus 210,000 observations over continents).

At the scale of TRANSCOM region (Table 3 and Figure 5), MERLIN (blue bars of Figure 5) does better than GOSAT (orange bars of Figure 5) on average and for most scenarios. Total residual errors are generally lower for MERLIN than for GOSAT for all TRANSCOM regions and most scenarios. This means that the impact of systematic errors is smaller for MERLIN than for GOSAT for all TRANSCOM regions and most scenarios. This is particularly visible for tropical continental regions (tropical South America, northern and southern Africa, and tropical Asia), for temperate South America, and for boreal Asia. The contrast between the performances achieved by the two instruments over tropical regions can be explained by differences in terms of the number of data available and by the stronger impact of systematic errors in the tropics for GOSAT.

However, overlapping of extreme scenarios indicates that some GOSAT scenarios do better than some MERLIN scenarios for some regions. For boreal North America and Australia, the mean residual error is larger (worse) for MERLIN than for GOSAT, but still, some of the MERLIN error scenarios perform as well as the worst GOSAT ones (boxplots overlap). This result is directly related to the choices made to distribute the systematic errors for the MERLIN mission and the penalty effect already described in the previous sections. We develop here a statistical approach for MERLIN as we do not have actual data as for GOSAT. Future refinements, possibly discarding some of the error scenarios, will occur when components of the instrument will be available allowing a more physical estimate of biases and their spatial distribution.

In terms of uncertainty reduction, it is interesting to compare the GOSAT performances estimated in this study with its actual performances derived from actual GOSAT observations. Using an objective approach (at least in principle), (Cressot et al., 2014) estimated the uncertainty reduction achieved when
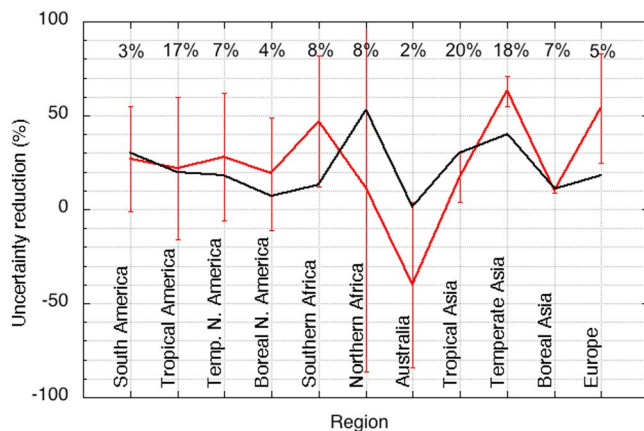
Figure 7. Mean uncertainty reduction for 11 regions mapping all continents (%) for this study (red line) and using GOSAT actual data (black line; Cressot et al., 2014). Errors bars on the red line represent 1 sigma standard deviations, calculated from the range provided by the 32 MERLIN error scenarios by considering that it represents 3 sigma values (99.7%). The percentages printed in the figure represent the mean fraction of global annual methane emissions from each region for the period 2003–2012, extracted from (Saunois et al., 2016) and also printed in the rightmost column of Table 3. The missing 1% in the total of percentages stands for oceanic emissions not plotted here. MERLIN = MEthane Remote LIdar missioN; GOSAT = Greenhouse Gases Observing SATellite.

assimilating actual GOSAT data in their inversion system (based on the retrievals of Parker et al., 2011, on a more recent version of LMDZ transport model and on a variational approach). The regional uncertainty reductions obtained here for GOSAT are consistent with those of Cressot et al. (2014; Table 3 and Figure 7). Although absolute values may differ slightly, regions with the highest uncertainty reductions (temperate Asia and Africa) and the lowest uncertainty reductions (boreal Asia, boreal North America, and Australia) are consistent in both studies. Residual errors are more degraded for Australia here (−40%) than in Cressot et al. (2014; 1%), suggesting again a possibly too pessimistic view here for the impact of systematic errors (for both GOSAT and MERLIN). However, a more optimistic view is also found for some other regions (e.g., Europe, South African regions, and South America) as compared to Cressot et al. (2014). Table 3 and Figure 7 also show the relative contribution of each region to global methane emissions in order to put uncertainty reductions in perspective. In this context, Australia, boreal North America, and boreal Asia only represent respectively 2%, 4%, and 7% of global emissions. The overall consistency between our work and Cressot et al. (2014) is satisfying for both studies and gives confidence that uncertainty reductions estimated here for GOSAT and MERLIN have the right order of magnitude.

4.4. Comparison Between Two Inversion Frameworks

Results of atmospheric inversions are primarily sensitive to the data assimilated, to the transport model used, and to their setup (e.g., Kirschke et al., 2013). Using the same set of random and systematic error data, we have performed an OSSE for MERLIN using the error scenario 28 and the two inversion frameworks based respectively on LMDZ (SIMGHG, see section 2) as previously, and on the TM3 transport model (MPI-Jena, see section 2). As systematic errors are the dominant factor contributing to total residual errors on methane emissions, we only compare here magnitudes and spatial distributions of the bias β_x on methane emissions obtained by SIMGHG and the MPI system, both forced by the bias scenario 28, for January and July (equation (4) and Figure 8).

The largest residual uncertainties in absolute values are located for the same regions for the two systems with positive values in equatorial Africa, in China, in central to eastern Europe, Canada, eastern tropical South America, and negative values in northern Africa, western tropical South America, India, and Bangladesh (July only). Temperate South America appears different between LMDZ and TM3, with positive values in LMDZ and more neutral values in TM3, in a region where coupling between atmospheric transport and contradictory systematic errors between land and ocean makes the results very sensitive as noticed in section 4.1.

At the scale of continental TRANSCOM regions, and on a yearly basis, biases have a similar sign for all regions but Australia, tropical Asia, and southern Africa, indicating a generally consistent conversion of the systematic errors on atmospheric columns into the emission space. Differences in tropical Africa and Asia may be due to the different convection schemes in the two transport models. Spatial and seasonal contrasts between regions are found to be larger for SIMGHG than for the MPI system (Figure 8, e.g., spatial dipoles in equatorial Africa and South America and seasonal dipoles in India or South America). This result may be explained by the fact that SIMGHG solves fluxes for 393 large regions only, whereas the MPI system solves fluxes at the transport model resolution (3,314 pixels). This means that SIMGHG scales up or down larger regions than the MPI system, possibly leading to larger residual emission biases. This is confirmed on a yearly basis with most residual biases inferred by SIMGHG being comparable to larger in absolute value than those inferred by the TM3 system, with the exceptions of tropical Asia and Australia. Indeed, the mean of positive biases at the scale of TRANSCOM regions is 0.7 mg $CH_4 \cdot m^{-2} \cdot day^{-1}$ for SIMGHG compared to only 0.2 mg $CH_4 \cdot m^{-2} \cdot day^{-1}$ for the MPI system. The consequence of this result, which needs to be confirmed by running more error scenarios in both systems in a future work, is that the uncertainty reductions presented in section 4.2 may be too pessimistic compared to those inferred by the MPI system.
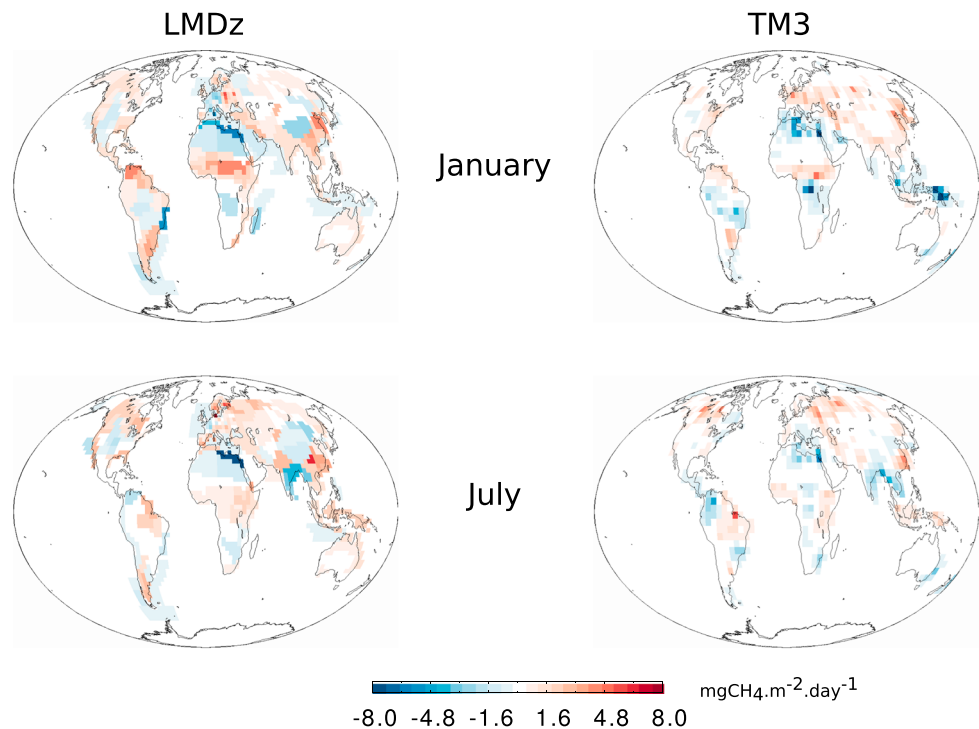
Figure 8. Comparison between LMDZ (left column) and TM3 (right column) for residual error statistics on methane emissions due to one scenario of systematic errors (mg $CH_4 \cdot m^{-2} \cdot day^{-1}$) for January (top row) and July (bottom row).

5. Conclusions

We have developed a first ensemble of scenarios to represent the expected random and systematic errors for the French-German project of space LIDAR MERLIN. We adopt a statistical approach based on physical assumptions where we identify, distribute in space and time, and combine causes of random and systematic errors on XCH_4 data. Thirty-two scenarios of systematic error have been produced and integrated with one scenario of random errors in the SIMGHG simulator in order to estimate their impact on the performance of MERLIN to reduce uncertainties on methane emissions from regional to global scale. MERLIN performances are also compared to those of GOSAT, the only shortwave infrared methane-dedicated instrument providing open-access data in 2017. The originality of our inverse method is to account for the impact of both random and systematic errors, therefore providing a more realistic and conservative view on the potential gain brought by satellite data, as compared to many previous analyses only accounting for the random part of the errors.

While almost 1 order of magnitude below the random errors in terms of parts per billion at the 50-km scale, XCH_4 systematic errors dominate the impact of MERLIN errors on the gain expected to improve regional methane emissions. At the global scale, the average uncertainty reduction is of +60% over continental regions (when Sahara and central Australia are removed from the analysis) but negative uncertainty reductions are found over oceanic regions indicating a major impact of systematic errors for these (low-emitting) regions. Some combination of systematic errors generate large penalties, for deserts when albedo and surface pressure effects have the same signs in the error combination, and for coastal regions of midlatitudes exposed to strong western winds, when albedo and surface pressure effects have opposite signs in the error combination.

At the scale of large continental regions, when removing desert areas (which have a negligible contribution to methane emissions), the average error reduction ranges from −132% (Australia) to +87% (temperate Asia). The largest uncertainty reductions are achieved for temperate (+84%) and for tropical regions (+56%). When aggregating all boreal continental regions, the average uncertainty reduction is +53%, indicating that MERLIN should bring significant constraints on average for the high latitudes, contrary to most current and

planned passive GHG missions. Accounting for all scenarios and among all continental regions out of deserts, only boreal North America appears strongly impacted by systematic errors. More work is needed to fully analyze the robustness of this result. The comparison with GOSAT reveals that MERLIN reduces uncertainties on methane emissions more than GOSAT for most regions, especially in the tropics. Finally, we note that the MPI inversion system, based on the TM3 transport model, suggests more optimistic uncertainty reductions.

The targeted systematic errors for MERLIN are particularly ambitious (±3.7 ppb) regarding actual systematic errors for past and current passive missions (Buchwitz et al., 2016). As shown by this work, MERLIN should allow improving our knowledge of methane emissions for most of the continental regions of the world. Still, even with such low values for systematic errors, their impact can be significant, possibly even canceling, in few regions, the gain brought by the MERLIN. Moreover, our choice of geophysical variables to distribute the plausible causes of error and the mathematical relations assumed between them (e.g., proportional) remains largely hypothetical. Other choices may change the expected performances.

These conclusions have to be moderated by the possibility that the comprehensive statistical approach developed here leads to a too pessimistic view for at least three reasons. First, the choice to distribute systematic errors on geophysical variables with a strong contrast between land and oceans largely drives the occurrence of negative uncertainty reduction. Although we know that MERLIN performances will be better over land than over oceans, this is a strong assumption that may be revisited while the instrument is built. Second, the combination of systematic causes of errors leading to the largest penalties (i.e., effects of albedo and surface pressure) may not be relevant in the end for MERLIN. Indeed, with the construction of the instrument ongoing, error scenarios will be refined and nonphysical scenarios excluded from future analyses. Third, it will probably be possible, during the construction of the instrument or during the mission, to identify and correct some of the systematic errors, as has been done for GOSAT.

Finally, TROPOMI on Sentinel 5P (Butz et al., 2012) will soon provide much more methane data than GOSAT, which will reduce the impact of random errors on the retrieval of methane emissions. However, to date, the magnitude of TROPOMI systematic errors is expected to be larger than GOSAT (European Space Agency, 2014). If confirmed, our results suggest that TROPOMI impact to reduce the uncertainties on methane emissions may be limited.

References

Alexe, M., Bergamaschi, P., Segers, A., Detmers, R., Butz, A., Hasekamp, O., et al. (2015). Inverse modelling of CH$_4$ emissions for 2010–2011 using different satellite retrieval products from GOSAT and SCIAMACHY. *Atmospheric Chemistry and Physics*, 15(1), 113–133. https://doi.org/10.5194/acp-15-113-2015

Bergamaschi, P., Frankenberg, C., Meirink, J. F., Krol, M., Dentener, F., Wagner, T., et al. (2007). Satellite chartography of atmospheric methane from SCIAMACHY on board ENVISAT: 2. Evaluation based on inverse model simulations. *Journal of Geophysical Research*, 112, D02304. https://doi.org/10.1029/2006JD007268

Bergamaschi, P., Frankenberg, C., Meirink, J. F., Krol, M., Villani, M. G., Houweling, S., et al. (2009). Inverse modeling of global and regional CH$_4$ emissions using SCIAMACHY satellite retrievals. *Journal of Geophysical Research*, 114, D22301. https://doi.org/10.1029/2009JD012287

Bergamaschi, P., Houweling, S., Segers, A., Krol, M., Frankenberg, C., Scheepmaker, R. A., et al. (2013). Atmospheric CH$_4$ in the first decade of the 21st century: Inverse modeling analysis using SCIAMACHY satellite retrievals and NOAA surface measurements. *Journal of Geophysical Research: Atmospheres*, 118, 7350–7369. https://doi.org/10.1002/jgrd.50480

Bergamaschi, P., Krol, M., Dentener, F., Vermeulen, A., Meinhardt, F., Graul, R., et al. (2005). Inverse modelling of national and European CH$_4$ emissions using the atmospheric zoom model TM5. *Atmospheric Chemistry and Physics*, 5(9), 2431–2460. https://doi.org/10.5194/acp-5-2431-2005

Bousquet, P., Ciais, P., Miller, J. B., Dlugokencky, E. J., Hauglustaine, D. A., Prigent, C., et al. (2006). Contribution of anthropogenic and natural sources to atmospheric methane variability. *Nature*, 443(7110), 439–443. https://doi.org/10.1038/nature05132

Buchwitz, M., de Beek, R., Noël, S., Burrows, J. P., Bovensmann, H., Schneising, O., et al. (2006). Atmospheric carbon gases retrieved from SCIAMACHY by WFM-DOAS: Version 0.5 CO and CH$_4$ and impact of calibration improvements on CO$_2$ retrieval. *Atmospheric Chemistry and Physics*, 6(9), 2727–2751. https://doi.org/10.5194/acp-6-2727-2006

Buchwitz, M., Dils, B., Boesch, H., Crevoisier, C., Detmers, R., Frankenberg, C., et al. (2016). Product validation and intercomparison report (PVIR) Rep., ESA Climate Change Initiative (CCI). Retrieved from http://www.esa-ghg-cci.org/?q=node/95

Burrows, J. P., Hölzle, E., Goede, A. P. H., Visser, H., & Fricke, W. (1995). SCIAMACHY—Scanning imaging absorption spectrometer for atmospheric chartography. *Acta Astronautica*, 35(7), 445–451. https://doi.org/10.1016/0094-5765(94)00278-T

Butz, A., Galli, A., Hasekamp, O., Landgraf, J., Tol, P., & Aben, I. (2012). TROPOMI aboard Sentinel-5 Precursor: Prospective performance of CH$_4$ retrievals for aerosol and cirrus loaded atmospheres. *Remote Sensing of Environment*, 120, 267–276. https://doi.org/10.1016/j.rse.2011.05.030

Butz, A., Guerlet, S., Hasekamp, O., Schepers, D., Galli, A., Aben, I., et al. (2011). Toward accurate CO$_2$ and CH$_4$ observations from GOSAT. *Geophysical Research Letters*, 38, L14812. https://doi.org/10.1029/2011GL047888

Butz, A., Hasekamp, O. P., Frankenberg, C., Vidot, J., & Aben, I. (2010). CH$_4$ retrievals from space-based solar backscatter measurements: Performance evaluation against simulated aerosol and cirrus loaded scenes. *Journal of Geophysical Research*, 115, D24302. https://doi.org/10.1029/2010JD014514

Chevallier, F. (2007). Impact of correlated observation errors on inverted CO_2 surface fluxes from OCO measurements. *Geophysical Research Letters*, *34*, L24804. https://doi.org/10.1029/2007GL030463

Chevallier, F., Breon, F. M., & Rayner, P. J. (2007). Contribution of the orbiting carbon observatory to the estimation of CO_2 sources and sinks: Theoretical study in a variational data assimilation framework. *Journal of Geophysical Research*, *112*, D09307. https://doi.org/10.1029/2006JD007375

Chevallier, F., Ciais, P., Conway, T. J., Aalto, T., Anderson, B. E., Bousquet, P., et al. (2010). CO_2 surface fluxes at grid point scale estimated from a global 21 year reanalysis of atmospheric measurements. *Journal of Geophysical Research*, *115*, D21307. https://doi.org/10.1029/2010JD013887

Chevallier, F., Maksyutov, S., Bousquet, P., Breon, F. M., Saito, R., Yoshida, Y., & Yokota, T. (2009). On the accuracy of the CO_2 surface fluxes to be estimated from the GOSAT observations. *Geophysical Research Letters*, *36*, L19807. https://doi.org/10.1029/2009GL040108

Ciais, P., Sabine, C., Bala, G., Bopp, L., Brovkin, V., Canadell, J., et al. (2013). Carbon and other biogeochemical cycles. In T. F. Stocker, et al. (Eds.), *Climate change 2013: The physical science basis. Contribution of Working Group I to the Fifth Assessment Report of the Intergovernmental Panel on Climate Change* (Chap. 6, pp. 465–570). Cambridge, UK and New York: Cambridge University Press.

Cressot, C., Chevallier, F., Bousquet, P., Crevoisier, C., Dlugokencky, E. J., Fortems-Cheiney, A., et al. (2014). On the consistency between global and regional methane emissions inferred from SCIAMACHY, TANSO-FTS, IASI and surface measurements. *Atmospheric Chemistry and Physics*, *14*(2), 577–592. https://doi.org/10.5194/acp-14-577-2014

Crevoisier, C., Nobileau, D., Fiore, A. M., Armante, R., Chedin, A., & Scott, N. A. (2009). Tropospheric methane in the tropics—First year from IASI hyperspectral infrared observations. *Atmospheric Chemistry and Physics*, *9*(17), 6337–6350. https://doi.org/10.5194/acp-9-6337-2009

Dee, D. P., Uppala, S. M., Simmons, A. J., Berrisford, P., Poli, P., Kobayashi, S., et al. (2011). The ERA-Interim reanalysis: Configuration and performance of the data assimilation system. *Quarterly Journal of the Royal Meteorological Society*, *137*(656), 553–597. https://doi.org/10.1002/qj.828

Dils, B., de Mazière, M., Müller, J. F., Blumenstock, T., Buchwitz, M., de Beek, R., et al. (2006). Comparisons between SCIAMACHY and ground-based FTIR data for total columns of CO, CH_4, CO_2 and N_2O. *Atmospheric Chemistry and Physics*, *6*(7), 1953–1976. https://doi.org/10.5194/acp-6-1953-2006

Dlugokencky, E. J., Nisbet, E. G., Fisher, R., & Lowry, D. (2011). Global atmospheric methane: Budget, changes and dangers. *Philosophical Transactions of the Royal Society A: Mathematical, Physical and Engineering Sciences*, *369*(1943), 2058–2072. https://doi.org/10.1098/rsta.2010.0341

Ehret, G., Bousquet, P., Pierangelo, C., Alpers, M., Millet, B., Abshire, J., et al. (2017). MERLIN: A French-German space lidar mission dedicated to atmospheric methane. *Remote Sensing*, *9*(10). https://doi.org/10.3390/rs9101052

Ehret, G., Kiemle, C., Wirth, M., Amediek, A., Fix, A., & Houweling, S. (2008). Space-borne remote sensing of CO_2, CH_4, and N_2O by integrated path differential absorption lidar: A sensitivity analysis. *Applied Physics B*, *90*(3-4), 593–608. https://doi.org/10.1007/s00340-007-2892-3

Emanuel, K. (1991). A scheme for representing cumulus convection in large-scale models. *Journal of the Atmospheric Sciences*, *48*(21), 2313–2329. https://doi.org/10.1175/1520-0469(1991)048<2313:ASFRCC>2.0.CO;2

European Space Agency (2014). Requirements for the geophysical validation of Sentinel-5 precursor products. ESA Repor. S5P-RS-ESA-SY-164, 21 May 2014 (45 pp.). Retrieved from https://earth.esa.int/pi/esa?id=3182&sideExpandedNavigationBoxId=Aos&cmd=image&topSelectedNavigationNodeId=AOS&targetIFramePage=/web/guest/pi-community/apply-for-data/ao-s&ts=1489486282962&type=file&colorTheme=03&sideNavigationType=AO&table=aotarget

Fix, A., Quatrevalet, M., Witschas, B., Wirth, M., Büdenbender, C., Amediek, A., & Ehret, G. (2015). Challenges and solutions for frequency and energy references for spaceborne and airborne integrated path differential absorption lidars. Paper presented at 27th International Laser Radar Conference (ILRC),NY, USA, 5–10 July 2015.

Frankenberg, C., Meirink, J. F., Bergamaschi, P., Goede, A. P. H., Heimann, M., Korner, S., et al. (2006). Satellite chartography of atmospheric methane from SCIAMACHY on board ENVISAT: Analysis of the years 2003 and 2004. *Journal of Geophysical Research*, *111*, D07303. https://doi.org/10.1029/2005JD006235

Frey, R. A., Ackerman, S. A., Liu, Y., Strabala, K. I., Zhang, H., Key, J. R., & Wang, X. (2008). Cloud detection with MODIS. Part I: Improvements in the MODIS cloud mask for collection 5. *Journal of Atmospheric and Oceanic Technology*, *25*(7), 1057–1072. https://doi.org/10.1175/2008jtecha1052.1

Geels, C., Gloor, M., Ciais, P., Bousquet, P., Peylin, P., Vermeulen, A. T., et al. (2007). Comparing atmospheric transport models for future regional inversions over Europe—Part 1: Mapping the atmospheric CO_2 signals. *Atmospheric Chemistry and Physics*, *7*(13), 3461–3479. https://doi.org/10.5194/acp-7-3461-2007

Gurney, K. R., Law, R. M., Denning, A. S., Rayner, P. J., Pak, B. C., Baker, D., et al. (2004). Transcom 3 inversion intercomparison: Model mean results for the estimation of seasonal carbon sources and sinks. *Global Biogeochemical Cycles*, *18*, GB1010. https://doi.org/10.1029/2003GB002111

Houweling, S., Aben, I., Breon, F. M., Chevallier, F., Deutscher, N., Engelen, R., et al. (2010). The importance of transport model uncertainties for the estimation of CO_2 sources and sinks using satellite measurements. *Atmospheric Chemistry and Physics*, *10*(20), 9981–9992. https://doi.org/10.5194/acp-10-9981-2010

Houweling, S., Breon, F. M., Aben, I., Rodenbeck, C., Gloor, M., Heimann, M., & Ciais, P. (2004). Inverse modeling of CO_2 sources and sinks using satellite data: A synthetic inter-comparison of measurement techniques and their performance as a function of space and time. *Atmospheric Chemistry and Physics*, *4*(2), 523–538. https://doi.org/10.5194/acp-4-523-2004

Houweling, S., Kaminski, T., Dentener, F., Lelieveld, J., & Heimann, M. (1999). Inverse modeling of methane sources and sinks using the adjoint of a global transport model. *Journal of Geophysical Research*, *104*(D21), 26,137–26,160. https://doi.org/10.1029/1999JD900428

Houweling, S., Krol, M., Bergamaschi, P., Frankenberg, C., Dlugokencky, E. J., Morino, I., et al. (2014). A multi-year methane inversion using SCIAMACHY, accounting for systematic errors using TCCON measurements. *Atmospheric Chemistry and Physics*, *14*(8), 3991–4012. https://doi.org/10.5194/acp-14-3991-2014

Hu, H., Hasekamp, O., Butz, A., Galli, A., Landgraf, J., Aan de Brugh, J., et al. (2016). The operational methane retrieval algorithm for TROPOMI. *Atmospheric Measurement Techniques*, *9*(11), 5423–5440. https://doi.org/10.5194/amt-9-5423-2016

Hungershoefer, K., Breon, F. M., Peylin, P., Chevallier, F., Rayner, P., Klonecki, A., et al. (2010). Evaluation of various observing systems for the global monitoring of CO_2 surface fluxes. *Atmospheric Chemistry and Physics*, *10*(21), 10,503–10,520. https://doi.org/10.5194/acp-10-10503-2010

Jacob, D. J., Turner, A. J., Maasakkers, J. D., Sheng, J., Sun, K., Liu, X., et al. (2016). Satellite observations of atmospheric methane and their value for quantifying methane emissions. *Atmospheric Chemistry and Physics*, *16*(22), 14,371–14,396. https://doi.org/10.5194/acp-16-14371-2016

Kiemle, C., Kawa, S. R., Quatrevalet, M., & Browell, E. V. (2014). Performance simulations for a spaceborne methane lidar mission. *Journal of Geophysical Research: Atmospheres*, *119*, 4365–4379. https://doi.org/10.1002/2013JD021253

Kiemle, C., Quatrevalet, M., Ehret, G., Amediek, A., Fix, A., & Wirth, M. (2011). Sensitivity studies for a space-based methane lidar mission. *Atmospheric Measurement Techniques*, *4*(10), 2195–2211. https://doi.org/10.5194/amt-4-2195-2011

Kirschke, S., Bousquet, P., Ciais, P., Saunois, M., Canadell, J. G., Dlugokencky, E. J., et al. (2013). Three decades of global methane sources and sinks. *Nature Geoscience*, *6*(10), 813–823. https://doi.org/10.1038/ngeo1955

Locatelli, R., Bousquet, P., Saunois, M., Chevallier, F., & Cressot, C. (2015). Sensitivity of the recent methane budget to LMDZ sub-grid-scale physical parameterizations. *Atmospheric Chemistry and Physics*, *15*(17), 9765–9780. https://doi.org/10.5194/acp-15-9765-2015

Meirink, J. F., Bergamaschi, P., Frankenberg, C., d'Amelio, M. T. S., Dlugokencky, E. J., Gatti, L. V., et al. (2008). Four-dimensional variational data assimilation for inverse modeling of atmospheric methane emissions: Analysis of SCIAMACHY observations. *Journal of Geophysical Research*, *113*, D17301. https://doi.org/10.1029/2007JD009740

Monteil, G., Houweling, S., Butz, A., Guerlet, S., Schepers, D., Hasekamp, O., et al. (2013). Comparison of CH_4 inversions based on 15 months of GOSAT and SCIAMACHY observations. *Journal of Geophysical Research: Atmospheres*, *118*, 11,807–811,823. https://doi.org/10.1002/2013jd019760

Morino, I., Uchino, O., Inoue, M., Yoshida, Y., Yokota, T., Wennberg, P. O., et al. (2011). Preliminary validation of column-averaged volume mixing ratios of carbon dioxide and methane retrieved from GOSAT short-wavelength infrared spectra. *Atmospheric Measurement Techniques*, *4*(6), 1061–1076. https://doi.org/10.5194/amt-4-1061-2011

Nisbet, E. G., Dlugokencky, E. J., & Bousquet, P. (2014). Methane on the rise—Again. *Science*, *343*(6170), 493–495. https://doi.org/10.1126/science.1247828

Nisbet, E. G., Dlugokencky, E. J., Manning, M. R., Lowry, D., Fisher, R. E., France, J. L., et al. (2016). Rising atmospheric methane: 2007–2014 growth and isotopic shift. *Global Biogeochemical Cycles*, *30*, 1356–1370. https://doi.org/10.1002/2016gb005406

O'Dell, C., Eldering, A., Crisp, D., Fisher, B., Gunson, M., McDuffie, J., et al. (2017). Recent improvements in XCO_2 measurements from OCO-2, 13th International Workshop on Greenhouse Gas Measurements from Space Edited, Helsinki, Finland.

Parker, R., Boesch, H., Cogan, A., Fraser, A., Feng, L., Palmer, P. I., et al. (2011). Methane observations from the Greenhouse Gases Observing SATellite: Comparison to ground-based TCCON data and model calculations. *Geophysical Research Letters*, *38*, L15807. https://doi.org/10.1029/2011GL047871

Patra, P. K., Houweling, S., Krol, M., Bousquet, P., Belikov, D., Bergmann, D., et al. (2011). TransCom model simulations of CH_4 and related species: Linking transport, surface flux and chemical loss with CH_4 variability in the troposphere and lower stratosphere. *Atmospheric Chemistry and Physics*, *11*(24), 12,813–12,837. https://doi.org/10.5194/acp-11-12813-2011

Pierangelo, C., Millet, B., Esteve, F., Alpers, M., Ehret, G., Flamant, P. H., et al. (2015). MERLIN (Methane Remote Sensing Lidar Mission): An overview, Paper presented at 27th International Laser Radar Conference, EPJ Web of Conferences, New York, July 5–10, 2015.

Prather, M. J., Holmes, C. D., & Hsu, J. (2012). Reactive greenhouse gas scenarios: Systematic exploration of uncertainties and the role of atmospheric chemistry. *Geophysical Research Letters*, *39*, L09803. https://doi.org/10.1029/2012GL051440

Remer, L. A., Kaufman, Y. J., Tanré, D., Mattoo, S., Chu, D. A., Martins, J. V., et al. (2005). The MODIS aerosol algorithm, products, and validation. *Journal of the Atmospheric Sciences*, *62*(4), 947–973. https://doi.org/10.1175/jas3385.1

Rodgers, C. D. (2000). *Inverse methods for atmospheric sounding: Theory and practice* (p. 240). Singapore, London: World Scientific. https://doi.org/10.1142/3171

Saunois, M., Bousquet, P., Poulter, B., Peregon, A., Ciais, P., Canadell, J. G., et al. (2016). The global methane budget 2000–2012. *Earth System Science Data*, *8*(2), 697–751. https://doi.org/10.5194/essd-8-697-2016

Saunois, M., Bousquet, P., Poulter, B., Peregon, A., Ciais, P., Canadell, J. G., et al. (2017). Variability and quasi-decadal changes in the methane budget over the period 2000–2012. *Atmospheric Chemistry and Physics*, *17*(18), 11,135–11,161. https://doi.org/10.5194/acp-17-11135-2017

Schaefer, H., Fletcher, S. E. M., Veidt, C., Lassey, K. R., Brailsford, G. W., Bromley, T. M., et al. (2016). A 21st century shift from fossil-fuel to biogenic methane emissions indicated by $^{13}CH_4$. *Science*, *352*(6281), 80–84. https://doi.org/10.1126/science.aad2705

Tiedtke, M. (1989). A comprehensive mass flux scheme for cumulus parameterization in large-scale models. *Monthly Weather Review*, *117*(8), 1779–1800. https://doi.org/10.1175/1520-0493(1989)117<1779:ACMFSF>2.0.CO;2

Wecht, K. J., Jacob, D. J., Sulprizio, M. P., Santoni, G. W., Wofsy, S. C., Parker, R., et al. (2014). Spatially resolving methane emissions in California: Constraints from the CalNex aircraft campaign and from present (GOSAT, TES) and future (TROPOMI, geostationary) satellite observations. *Atmospheric Chemistry and Physics*, *14*(15), 8173–8184. https://doi.org/10.5194/acp-14-8173-2014

Wunch, D., Toon, G. C., Blavier, J.-F. L., Washenfelder, R. A., Notholt, J., Connor, B. J., et al. (2011). The Total Carbon Column Observing Network. *Philosophical Transactions of the Royal Society A: Mathematical, Physical and Engineering Sciences*, *369*(1943), 2087–2112. https://doi.org/10.1098/rsta.2010.0240